

Beam-normal single-spin asymmetry in elastic scattering of electrons from a spin-0 nucleus

Oleksandr Koshchii^a, Mikhail Gorchtein^b, Xavier Roca-Maza^c, Hubert Spiesberger^a

^a*PRISMA⁺ Cluster of Excellence, Institut für Physik,*

Johannes Gutenberg-Universität, D-55099 Mainz, Germany

^b*PRISMA⁺ Cluster of Excellence, Institut für Kernphysik,*

Johannes Gutenberg-Universität, D-55099 Mainz, Germany

^c*Dipartimento di Fisica, Università degli Studi di Milano, Via Celoria 16, I-20133 Milano, Italy
and INFN, Sezione di Milano, Via Celoria 16, I-20133 Milano, Italy*

(Dated: January 5, 2022)

We study the beam-normal single-spin asymmetry (BNSSA) in high-energy elastic electron scattering from several spin-0 nuclei. Existing theoretical approaches work in the plane-wave formalism and predict the BNSSA to scale as $\sim A/Z$ with the atomic number Z and nuclear mass number A . While this prediction holds for light and intermediate nuclei, a striking disagreement in both the sign and the magnitude of BNSSA was observed by the PREX collaboration for ^{208}Pb , coined the “PREX puzzle”. To shed light on this disagreement, we go beyond the plane-wave approach which neglects Coulomb distortions known to be significant for heavy nuclei. We explicitly investigate the dependence of BNSSA on A and Z by i) including inelastic intermediate states’ contributions into the Coulomb problem in the form of an optical potential, ii) by accounting for the experimental information on the A -dependence of the Compton slope parameter, and iii) giving a thorough account of the uncertainties of the calculation. Despite of these improvements, the PREX puzzle remains unexplained. We discuss further strategies to resolve this riddle.

I. INTRODUCTION

Corrections due to two-photon exchange (TPE) Feynman diagrams for electron scattering have received considerable interest in recent years [1–12], primarily in the context of the discrepancy of the experimental results [13, 14] for the electric-to-magnetic form factor ratio, which sometimes is referred to as the proton form factor puzzle. There are strong indications [15] that this puzzle can be resolved by a proper inclusion of TPE in the experimental analysis. In view of the interest in TPE, beam- and target-normal single spin asymmetries (SSAs) in elastic electron-nucleus (eN) scattering regained attention of theorists [16–27]. It has been known for several decades that these transverse asymmetries are T-odd observables which, in the absence of CP violation, are sensitive to the imaginary part of the scattering amplitude [28]. The T-even one-photon exchange amplitude (in the plane-wave Born approximation, PWBA) is purely real, and it is the T-odd imaginary (absorptive) part of the TPE amplitude that gives rise to nonzero transverse asymmetries.

The measurement of the BNSSA (Mott asymmetry, Sherman function and analyzing power are alternative names which are more common for low-energy electron scattering) has been part of the parity-violation program over the past two decades [29–38]. Parity violation is observed in eN scattering when the incoming electron beam is longitudinally polarized. Measurements of the respective parity-violating (PV) asymmetry have far-reaching applications, including precision tests of the Standard Model [39–41] and studies of the nuclear structure [42–45]. Typical values of the PV asymmetry range from parts per million to parts per billion, several orders of

magnitude below BNSSA, hence a thorough control of this source of a potentially significant systematical uncertainty associated with an unknown transverse component of the electron beam polarization has become a must-do in the analyses of PV electron scattering. Thanks to the fact that these experiments are designed for measuring the much smaller PV asymmetry, in the past decades good-quality data of the BNSSA have become available in a variety of kinematic regions and for a variety of targets.

The general theoretical treatment of transverse asymmetries in high-energy ($E_b \gtrsim 1$ GeV) elastic eN scattering is a highly challenging task. The two approaches that have been pursued in the literature in this energy range are i) solving the Dirac equation for the electron moving in the Coulomb field of an infinitely heavy nucleus in the distorted-wave Born approximation (DWBA) upon neglecting nuclear and hadronic excitations of the intermediate states [21]; and ii) including the latter only in the approximation of the two-photon exchange [24], disregarding multi-photon exchange effects. The former approach enables one to accurately account for Coulomb distortion effects which scale with the nuclear charge, $Z\alpha$, and thus are important for electron scattering from heavy nuclei. While this mechanism dominates at electron energies in the few-MeV range, its contribution to BNSSA drops with the electron energy, and for GeV electrons the inelastic hadronic contribution exceeds the former by several orders of magnitude [24]. When compared with the corresponding scattering data from Jefferson Lab [34] and MAMI [37, 38], the second approach has been quite successful for light and intermediate-mass nuclei, e.g. ^4He , ^{12}C , ^{28}Si , and ^{90}Zr , while a stark disagreement between theory and experiment for BNSSA on the ^{208}Pb target

[34], sometimes called the ‘‘PREX puzzle’’, was observed. This disagreement indicates that the theoretical calculation of Ref. [24] may miss some important nuclear contributions which become important for very heavy nuclei, while only playing a minor role otherwise. One such effect might be the exchange of many soft Coulomb photons on top of the two-photon exchange which may lead to a substantial modification of the leading-order result.

In this article, we join the two aforementioned approaches. We include the contribution of the inelastic hadronic states as an optical potential entering the Dirac equation and study the interplay of the Coulomb distortion and two-photon exchange within one formalism. We also improve the existing calculations by using a more extensive database for experimental information on Compton scattering on nuclei. We use this information to extract the dependence of the optical potential on the nuclear mass number.

II. DIRAC COULOMB PROBLEM AT RELATIVISTIC ENERGIES

We consider elastic scattering of an electron of mass m by a spin-0 nucleus of mass M ,

$$e^-(k_1, S_i) + N(p_1) \rightarrow e^-(k_2, S_f) + N(p_2), \quad (1)$$

where k_1 (k_2) and p_1 (p_2) denote the four-momenta of the initial (final) electron and initial (final) nucleus, and S_i (S_f) describes the spin projection of the initial (final) electron along the considered axis.

The beam-normal single-spin asymmetry is defined as

$$B_n \equiv \frac{\sigma_\uparrow - \sigma_\downarrow}{\sigma_\uparrow + \sigma_\downarrow}, \quad (2)$$

where σ_\uparrow (σ_\downarrow) represents the eN scattering cross section for electrons with spin parallel (anti-parallel) to the normal vector ξ^μ given by

$$\xi^\mu = (0, \vec{\xi}), \quad \vec{\xi} \equiv \frac{\vec{k}_1 \times \vec{k}_2}{|\vec{k}_1 \times \vec{k}_2|}. \quad (3)$$

In order to account for Coulomb distortion and inelastic intermediate excitations in the considered scattering process, we solve the relativistic Dirac equation¹:

$$\left(-i\vec{\alpha} \cdot \vec{\nabla} + \beta m + V_c + i\beta V_{\text{abs}} \right) \Psi(\vec{r}) = E \Psi(\vec{r}), \quad (4)$$

where $\vec{\alpha} = \gamma_0 \vec{\gamma}$ and $\beta = \gamma_0$ are Dirac matrices, and E the electron energy in the center of mass reference frame related (neglecting the electron mass) to the laboratory energy E_b by $E = E_b / \sqrt{1 + 2E_b/M}$.

The Coulomb potential $V_c(r)$ corresponds to the nuclear charge distribution which is known from electron scattering experiments [46]. The absorptive potential $V_{\text{abs}}(r, E)$ represents the contribution of the inelastic hadronic excitations in the two-photon exchange diagram, as discussed in detail in Sec. III. The inclusion of the absorptive component of the potential in the Dirac problem is the main novel feature of this work. Note that the form of this potential, $i\beta V_{\text{abs}}$, is specific to the problem at hand: an absorptive potential of the form $i\tilde{V}_{\text{abs}}$ only contributes to B_n at higher order in α , exceeding the precision goal of this study. Spherically symmetric $V_c(r)$ and $V_{\text{abs}}(r, E)$ should be expected for spin-0 nuclei, and we use this assumption throughout this paper.

For electron scattering in a central field, the solution of the Dirac equation can be expanded in spherical waves [47],

$$\Psi_{\kappa, m_z}(\vec{r}) = \frac{1}{r} \begin{pmatrix} P_\kappa(r) \Omega_{\kappa, m_z}(\theta, \phi) \\ iQ_\kappa(r) \Omega_{-\kappa, m_z}(\theta, \phi) \end{pmatrix}, \quad (5)$$

where $\Omega_{\kappa, m_z}(\theta, \phi)$ are 2-component spherical spinors. The relativistic quantum number κ takes values κ_1 and κ_2 given by

$$\begin{cases} \kappa_1 = -(j + 1/2) & \text{if } j = l + 1/2, \\ \kappa_2 = +(j + 1/2) & \text{if } j = l - 1/2, \end{cases} \quad (6)$$

where l, j , and m_z are the orbital angular momentum, total angular momentum, and total angular momentum projection quantum numbers, respectively.

The radial functions $P_\kappa(r)$ and $Q_\kappa(r)$ satisfy the following coupled system of differential equations:

$$\begin{aligned} \frac{dP_\kappa}{dr} &= -\frac{\kappa}{r} P_\kappa + \left(E - V_c + iV_{\text{abs}} + m \right) Q_\kappa, \\ \frac{dQ_\kappa}{dr} &= -\left(E - V_c - iV_{\text{abs}} - m \right) P_\kappa + \frac{\kappa}{r} Q_\kappa. \end{aligned} \quad (7)$$

We normalize the spherical waves such that the radial function $P_\kappa(r)$ oscillates asymptotically with unit amplitude,

$$P_\kappa(r \rightarrow \infty) = \sin \left(kr - l\frac{\pi}{2} - \eta \ln 2kr + \delta_\kappa \right), \quad (8)$$

where k is the electron’s wave number and $\eta = -Z\alpha E/k$ is the relativistic Sommerfeld parameter. The scattering phase shift δ_κ is obtained by requiring continuity of the radial function $P_\kappa(r)$ and its derivative at large distance r_m (matching distance), at which the numerical solution of Eq. (7) is matched to the known analytical solution of the Dirac equation for a point-like Coulomb potential, $V_{\text{pc}}(r) = -Z\alpha/r$. The matching at large distances is justified by the fact that both the absorptive potential and the short range part of the Coulomb potential can be neglected beyond r_m . As a result, the solution of the point-like Coulomb potential provides the proper asymptotic behavior.

¹ We use natural units throughout this paper.

The absorptive potential, while having a shorter range than the Coulomb one, turns out to extend to distances of the order of the inverse electron mass $1/m \sim 400$ fm, and the respective computation becomes cumbersome (details are discussed in Sec. III C). To perform the numerical calculation, we use the ELSEPA package [47, 48], properly modified to include the absorptive potential.

Knowledge of the phase shift enables one to determine the direct and spin-flip scattering amplitudes, $f(\theta)$ and $g(\theta)$, respectively, in terms of which the beam-normal SSA is given by

$$B_n = i \frac{f(\theta)g^*(\theta) - f^*(\theta)g(\theta)}{|f(\theta)|^2 + |g(\theta)|^2} = \frac{2\text{Im}[f^*(\theta)g(\theta)]}{|f(\theta)|^2 + |g(\theta)|^2}. \quad (9)$$

These amplitudes admit the following partial-wave expansions:

$$f(\theta) = \frac{1}{2ik} \sum_{l=0}^{\infty} [(l+1)(e^{2i\delta_{\kappa_1}} - 1) + l(e^{2i\delta_{\kappa_2}} - 1)] P_l(\cos\theta),$$

$$g(\theta) = \frac{1}{2ik} \sum_{l=0}^{\infty} [e^{2i\delta_{\kappa_2}} - e^{2i\delta_{\kappa_1}}] P_l^1(\cos\theta), \quad (10)$$

where $P_l(\cos\theta)$ and $P_l^1(\cos\theta)$ are Legendre and associated Legendre polynomials. The series in Eqs. (10) is singular at $\theta = 0$ leading to a slow convergence when approaching that limit. The convergence of the series can be accelerated by using the reduced series method suggested by Yennie et al. in Ref. [49]. This method prescribes to reduce the degree of the singularity of the original series by expanding $(1 - \cos\theta)^n f(\theta)$ and $(1 - \cos\theta)^n g(\theta)$ into analogous sums over Legendre polynomials. The new sums converge more quickly, however the extraction of the original amplitudes requires to divide by a factor $(1 - \cos\theta)^n$. As a result, for forward scattering the use of too many reductions becomes unstable. We found the optimal number of reductions to be $n=2$.

III. ABSORPTIVE POTENTIAL FROM THE TWO-PHOTON EXCHANGE

A. Elastic eN scattering

We turn to a field-theoretical description of the eN scattering process to deduce the explicit form of the potentials in Eq. (4). In the absence of P- and CP-violation, the invariant amplitude describing the scattering process Eq. (1) for a spin-0 nucleus has two terms, [24],

$$T = \frac{e^2}{|t|} \bar{u}(k_2) \left[mA_1(s, t) + (\not{p}_1 + \not{p}_2)A_2(s, t) \right] u(k_1), \quad (11)$$

with the usual Mandelstam invariants $t = (k_1 - k_2)^2$ and $s = (k_1 + p_1)^2$, and two scalar amplitudes A_1 and A_2 .

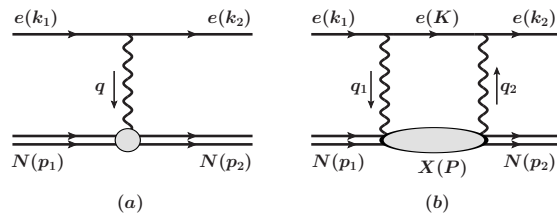


FIG. 1. (a) One- and (b) two-photon exchange diagrams for elastic electron-nucleus scattering.

The initial and final electron Dirac spinors are denoted by $u(k_1)$ and $u(k_2)$, respectively.

In the static approximation, $|t| \ll s$, M^2 , E^2 , relativistic electron-nucleus scattering reduces to the problem of potential scattering of a relativistic electron in the field of a static nucleus. In the static limit, $p_1 = p_2 = (M, 0)$, we can rewrite Eq. (11) as

$$T = 2Mu^\dagger(k_2) \left[\frac{e^2}{|t|} \left(\frac{m\beta}{2M} A_1 + A_2 \right) \right] u(k_1). \quad (12)$$

To leading order in $Z\alpha$, the electron-nucleon interaction proceeds via the exchange of a virtual photon, cf. Fig. 1(a), and only the amplitude A_2 survives at this order,

$$A_1^{1\gamma} = 0, \quad A_2^{1\gamma} = ZF_{\text{ch}}(t). \quad (13)$$

Here, F_{ch} denotes the nuclear charge form factor, which is related to the spatial distribution of the nuclear charge $\rho_{\text{ch}}(r)$ by a three-dimensional Fourier transform,

$$F_{\text{ch}}(t) = \int \rho_{\text{ch}}(r) e^{-i\vec{q}\cdot\vec{r}} d^3\vec{r}, \quad \text{with } |\vec{q}| \equiv \sqrt{|t|}, \quad (14)$$

with the normalization $\int \rho_{\text{ch}}(r) d^3\vec{r} = 1$.

The T-odd observable B_n is determined by the imaginary part of the interference of A_1 and A_2 [28]. An imaginary part, $\text{Im}A_1$, for elastic eN scattering, i.e. for $s > M^2$, $t < 0$, appears first at next-to-leading order in $Z\alpha$ in the two-photon exchange contribution depicted in Fig. 1(b).

The absorptive and Coulomb components of the total potential which enter the Dirac equation (4), V_{abs} and V_{c} , are related to $\text{Im}A_1$ and A_2 through a three-dimensional Fourier transform of the first and second terms in square brackets of Eq. (12). Including the leading nonvanishing terms in the perturbative expansion of these amplitudes we obtain

$$V_{\text{c}}(r) = - \int \frac{d^3\vec{q}}{(2\pi)^3} \frac{e^2}{\vec{q}^2} A_2^{1\gamma} e^{i\vec{q}\cdot\vec{r}} = -Z\alpha \int d^3\vec{r}' \frac{\rho_{\text{ch}}(\vec{r}')}{|\vec{r}' - \vec{r}'|}, \quad (15)$$

$$V_{\text{abs}}(r, E_{\text{b}}) = - \int \frac{d^3\vec{q}}{(2\pi)^3} \frac{e^2}{\vec{q}^2} \frac{m}{2M} \text{Im}A_1^{2\gamma} e^{i\vec{q}\cdot\vec{r}}. \quad (16)$$

Other contributions, e.g. recoil corrections and higher-order contributions to A_2 , are neglected here. In the next

section we are going to study the perturbative result for the two-photon exchange diagram in order to determine an explicit ansatz for the absorptive potential.

B. Imaginary part of the two-photon exchange amplitude

The imaginary part of the two-photon exchange amplitude, displayed in Fig. 1(b), is given by

$$\text{Im}T_{2\gamma} = e^4 \int \frac{d^3\vec{K}}{(2\pi)^3 2E_K} \frac{2\pi L_{\alpha\beta} W^{\alpha\beta}}{Q_1^2 Q_2^2}, \quad (17)$$

where the momenta are defined as shown in Fig. 1, with $Q_{1,2}^2 = -q_{1,2}^2 = -(k_{1,2} - K)^2$, and E_K and \vec{K} the energy and three-momentum of the intermediate electron inside the loop, respectively. The leptonic tensor $L_{\alpha\beta}$ reads

$$L_{\alpha\beta} = \bar{u}(k_2)\gamma_\alpha(\not{K} + m)\gamma_\beta u(k_1), \quad (18)$$

and the doubly virtual Compton scattering (VVCS) tensor $W^{\alpha\beta}$ is defined as

$$\begin{aligned} W^{\alpha\beta} &\equiv \frac{1}{4\pi} \sum_X \langle p_2 | J_\alpha^\dagger(0) | X(P) \rangle \langle X(P) | J_\beta(0) | p_1 \rangle \quad (19) \\ &\quad \times (2\pi)^4 \delta^4(p_2 + q_2 - P) \\ &= \frac{1}{4\pi} \int d^4x e^{iq_2x} \langle p_2 | [J^{\alpha\dagger}(x), J^\beta(0)] | p_1 \rangle, \quad (20) \end{aligned}$$

where \sum_X in Eq. (19) includes the phase-space integral $\int d^3\vec{P}/((2\pi)^3 2E_P)$. We note that in order to get from Eq. (19) to Eq. (20) one can apply a translation to the current operator, $J_\alpha(x) = e^{iPx} J_\alpha(0) e^{-iPx}$, and $(2\pi)^4 \delta^4(p_2 + q_2 - P) = \int d^4x e^{i(p_2 + q_2 - P)x}$. The matrix element of the hadronic current for the elastic intermediate state is given by $\langle P | J_\beta(0) | p_1 \rangle = (P + p_1)_\beta Z F_{\text{ch}}(Q_1^2)$.

To compute the imaginary part of the TPE diagram and perform a systematic study of its uncertainties, we note that the result of the contraction with the leptonic tensor can be decomposed into two parts,

$$L_{\alpha\beta} W^{\alpha\beta} = m \bar{u}(k_2) u(k_1) \mathcal{A}_1 + \bar{u}(k_2) (\not{p}_1 + \not{p}_2) u(k_1) \mathcal{A}_2, \quad (21)$$

where \mathcal{A}_1 and \mathcal{A}_2 are analytical functions of t , Q_1^2 , Q_2^2 , $W^2 = (p_1 + q_1)^2$ and s . With this notation, a straightforward connection to the amplitude A_1 can be made,

$$\text{Im}A_1^{2\gamma} = \frac{\alpha|t|}{2\pi} \int \frac{\vec{K}^2 d\vec{K}}{E_K Q_1^2 Q_2^2} \mathcal{A}_1(t, Q_1^2, Q_2^2, W^2, s). \quad (22)$$

In the following we will obtain the long-range (i.e. low- t) behavior of $\text{Im}A_1^{2\gamma}$, adequate for devising the form of the absorptive potential via Eq. (16).

To that end, we follow Refs. [16–18] which observed that B_n is logarithmically enhanced in the kinematical

regime $m^2 \ll |t| \ll s$ due to the collinear photon singularity. The integrals over the solid angle that are prone to this enhancement read

$$\begin{aligned} I_0 &= \frac{|t|\vec{K}^2}{2\pi} \int \frac{d\Omega_K}{Q_1^2 Q_2^2} \approx \ln \frac{|t|}{m^2}, \\ I_1 &= \frac{E|\vec{K}|}{\pi} \int \frac{d\Omega_K}{Q_1^2} = \frac{E|\vec{K}|}{\pi} \int \frac{d\Omega_K}{Q_2^2} \approx \ln \frac{4E^2}{m^2}, \quad (23) \end{aligned}$$

with the energies $E = (s - M^2)/(2\sqrt{s})$ and $E_K = (s - W^2)/(2\sqrt{s})$ defined in the center-of-mass frame, and $|\vec{K}| = \sqrt{E_K^2 - m^2}$. Here we have listed only the leading behavior in the limit where $\sqrt{|t|}$ and E are large compared with the electron mass m . The exact expressions are given in the Appendix A. For the values we are interested in, $|t| \approx 0.01 \text{ GeV}^2$, the first logarithm is of order 10. The second logarithm is of order 25 for E in the GeV range, but is suppressed by an explicit factor $|t|$ with respect to the former. This hierarchy defines our approximation scheme:

$$\text{Im}A_1^{2\gamma} = \alpha \int \frac{d|\vec{K}|}{E_K} \left[\mathcal{A}_1^{(0)}(t) I_0 + |t| \frac{E_K}{2E} \mathcal{A}_1^{(1)}(t) I_1 + \dots \right], \quad (24)$$

where terms denoted by dots are doubly suppressed: they contain one power of t and no large logarithm. To arrive at this result we have used an expansion in small photon virtualities,

$$\mathcal{A}_1(t, Q_1^2, Q_2^2, W^2, s) = \mathcal{A}_1^{(0)}(t) + \frac{Q_1^2 + Q_2^2}{2} \mathcal{A}_1^{(1)}(t) + \dots, \quad (25)$$

where we show explicitly only the dependence of $\mathcal{A}_1^{(0)}$ and $\mathcal{A}_1^{(1)}$ on t , while their dependence on the other four invariant variables is implicitly assumed. For consistency, we will only keep the ‘‘strong’’ t -dependence in $\mathcal{A}_1^{(0)}$, $\mathcal{A}_1^{(1)}$, e.g. an exponential or the nuclear charge form factor, but will neglect power corrections $\sim t/M^2$, t/s , t/E^2 . In the literature only $\mathcal{A}_1^{(0)}(t)$ has been obtained in the near-forward limit. In this work we include the second term and use it to estimate the uncertainty induced by the approximations used.

Next we proceed to derive explicit expressions for $\mathcal{A}_1^{(0)}$ and $\mathcal{A}_1^{(1)}$. The optical theorem relates them to the total cross sections for virtual photoabsorption at the first step. The t -dependence is reconstructed at the second step from the measured differential cross section for real Compton scattering. This two-step procedure requires that we operate with the Compton amplitudes which are well-defined in both

- the forward scattering limit, described by $t = 0$ and finite $Q_1^2 = Q_2^2 \equiv Q^2$, and
- the real Compton scattering limit, described by $Q_1^2 = Q_2^2 = 0$ and finite t .

The general virtual Compton tensor $W^{\alpha\beta}$ for a spinless target consists of five independent Lorentz structures, $\tau_i^{\alpha\beta}$, ($i = 1, \dots, 5$) [50–52] multiplied by respective scalar amplitudes $\mathcal{F}_i(t, Q_1^2, Q_2^2, W^2)$. In the approximation scheme we work in, the number of structures that contribute is further reduced upon neglecting terms that vanish in both the forward and the real Compton scattering limits. This restricts our consideration to just two structures $\tau_i^{\alpha\beta}$ (in the original enumeration of Ref. [50]):

$$\begin{aligned} W^{\alpha\beta} &= \tau_1^{\alpha\beta} \text{Im } \mathcal{F}_1 + \tau_3^{\alpha\beta} \text{Im } \mathcal{F}_3, \\ \tau_1^{\alpha\beta} &= (q_1 \cdot q_2) g^{\alpha\beta} - q_1^\alpha q_2^\beta, \\ \tau_3^{\alpha\beta} &= (\bar{p} \cdot \bar{q})^2 g^{\alpha\beta} - (\bar{p} \cdot \bar{q})(\bar{p}^\beta q_1^\alpha + \bar{p}^\alpha q_2^\beta) \\ &\quad + (q_1 \cdot q_2) \bar{p}^\alpha \bar{p}^\beta, \end{aligned} \quad (26)$$

with $\bar{p} = (p_1 + p_2)/2$ and $\bar{q} = (q_1 + q_2)/2$. Other structures (explicitly provided in Ref. [50]) surviving in the forward limit for virtual photons can always be expressed as linear combinations of $\tau_{1,3}$.

By contracting the leptonic and virtual Compton tensors, we find an explicit expression for \mathcal{A}_1 ,

$$\begin{aligned} \mathcal{A}_1(t) &= \text{Im } \mathcal{F}_1 [(Q_1^2 + Q_2^2)(\lambda - 2) - t] \\ &\quad + \text{Im } \mathcal{F}_3 [(4(\bar{p} \cdot \bar{q})(\bar{p} \cdot \bar{k}) - \bar{p}^2(q_1 \cdot q_2)) \\ &\quad \times (\lambda - 1) - 2(\bar{p} \cdot \bar{q})^2(\lambda - 2)], \end{aligned} \quad (27)$$

where $\bar{k} = (k_1 + k_2)/2$ and

$$\lambda = \frac{2(s - M^2)(s - W^2) - (Q_1^2 + Q_2^2)(s + M^2)}{2(s - M^2)^2}.$$

The forward limit of the amplitudes $\mathcal{F}_{1,3}$ is determined by the usual structure functions F_1 and F_2 ,

$$\begin{aligned} Q^2 \text{Im } \mathcal{F}_1(0, Q^2, Q^2, W^2) &= F_1 - \frac{1}{2x_{\text{Bj}}} F_2 \equiv F_L, \\ Q^2 \text{Im } \mathcal{F}_3(0, Q^2, Q^2, W^2) &= -\frac{1}{(\bar{p} \cdot \bar{q})} F_2, \end{aligned} \quad (28)$$

where $x_{\text{Bj}} = Q^2/(2\bar{p} \cdot \bar{q})$. The structure functions are related to the transverse and longitudinal inelastic virtual photoabsorption cross sections σ_T and σ_L via

$$\begin{aligned} F_1(W^2, Q^2) &= \frac{W^2 - M^2}{8\pi^2\alpha} \sigma_T(W^2, Q^2), \\ F_2(W^2, Q^2) &= \frac{W^2 - M^2}{8\pi^2\alpha} \frac{Q^2(\bar{p} \cdot \bar{q})}{(\bar{p} \cdot \bar{q})^2 + Q^2 M^2} \\ &\quad \times (\sigma_T(W^2, Q^2) + \sigma_L(W^2, Q^2)). \end{aligned} \quad (29)$$

Expanding $\sigma_{T,L}$ at $Q^2 = 0$ we obtain the following expressions for $\mathcal{A}_1^{(0)}$ and $\mathcal{A}_1^{(1)}$:

$$\mathcal{A}_1^{(0)}(0) = \frac{M}{2\pi^2\alpha} E_K \frac{\omega}{E} \sigma_T^0(\omega), \quad (30)$$

$$\begin{aligned} \mathcal{A}_1^{(1)}(0) &= \frac{M}{2\pi^2\alpha} \left[\left(-\frac{2}{\omega} + \frac{3}{2E_b} - \omega \frac{(E_b + M)}{2ME_b^2} \right) \sigma_T^0(\omega) \right. \\ &\quad \left. + E_K \frac{\omega}{E} \sigma_T'(\omega) + 2\omega \sigma_L'(\omega) \right], \end{aligned} \quad (31)$$

where $E_b = (s - M^2)/(2M)$ and instead of the variable W^2 we used $\omega = (W^2 - M^2)/(2M)$. Moreover, $\sigma_T^0(\omega) \equiv \sigma_T(\omega, Q^2 = 0)$ and $\sigma_{T,L}'(\omega) \equiv d\sigma_{T,L}/dQ^2(\omega, Q^2 = 0)$.

The t -dependence of the Compton amplitudes can be retrieved from experimental studies of the differential cross section for Compton scattering. Measurements are available at high energies, $E \sim 3 - 5$ GeV and at low $-t$, $0.001 < -t < 0.06$ GeV², see Refs. [53, 54]. In this kinematic range,

$$\frac{d\sigma}{dt} \approx \frac{\pi\alpha^2 M^2 \omega^2}{16} |\text{Im } \mathcal{F}_3|^2 (1 + R^2), \quad (32)$$

where the terms suppressed with powers of t were neglected, and we defined $R = |\text{Re } \mathcal{F}_3|/|\text{Im } \mathcal{F}_3|$. The data follow an exponential fall-off,

$$\frac{d\sigma}{dt}(\omega, t) = a e^{-B|t|} F_{\text{ch}}^2(t) + \sigma_{\text{inc}}. \quad (33)$$

$F_{\text{ch}}(t)$ is the nuclear charge form factor. Depending on the nucleus, we adopt a two-parameter Fermi model (¹⁹⁷Au, ¹⁰⁹Ag, and ⁶⁴Cu), a Fourier-Bessel model (⁴⁹Ti, ²⁷Al, and ¹²C), or a sum of Gaussians (⁴He) [46, 55, 56]. A (small) incoherent contribution σ_{inc} was added to improve the description of the data around the first diffraction minimum and above. In the t -range of interest this contribution is a slowly-varying function of t which can be approximated by a polynomial. In practice, we found that only the constant term is reliably constrained by the data. This is related to the rather small range of t where data are available, as well as large uncertainties at the largest values of the momentum transfer. We perform the fit using the 3 GeV and 5 GeV data of Ref. [54] with B and σ_{inc} as free parameters, and fix the normalization of the coherent contribution a such that the sum $a + \sigma_{\text{inc}}$ reproduces the values of $d\sigma/dt(0)$ reported in Ref. [54].

We find the incoherent contributions to be irrelevant for the description of the data at 3 GeV and set σ_{inc} to 0 (cf. second column of Table I). For the 5 GeV data, instead, its inclusion greatly improves the overall fit due to a larger measured t -range. Importantly, however, whether including or excluding the incoherent contribution from the fit barely affects the extracted value of B , as the latter is determined by low- t data. For the ⁴He data of Ref. [53], we treat a as a free parameter. The extracted values for a , B , and σ_{inc} are listed in Table I. We display the fit of the 5 GeV data of Ref. [54] in Fig. 2.

In the literature, BNSSA measurements have been reported for the following spin-0 nuclei: ⁴He, ¹²C, ²⁸Si, ⁴⁰Ca, ⁴⁸Ca, ⁹⁰Zr and ²⁰⁸Pb. To obtain the slope parameter B for ²⁸Si, ⁴⁰Ca, ⁴⁸Ca, ⁹⁰Zr and ²⁰⁸Pb for which no direct data is available, we use the values obtained for nuclei with the closest atomic weight in Table I. More specifically, we use the values of B from ²⁷Al for ²⁸Si, ⁴⁹Ti for ^{40,48}Ca, ¹⁰⁹Ag for ⁹⁰Zr, and ¹⁹⁷Au for ²⁰⁸Pb. Values of B obtained from the fit to Compton data at $\omega = 3$ GeV and $\omega = 5$ GeV are compatible with each other (where a comparison is possible). We use the more

TABLE I. Average values and corresponding theoretical uncertainties for the Compton slope parameter B extracted from Compton scattering data of Refs. [53] and [54]. For nuclei with $A \geq 12$, $d\sigma/dt(0) = a + \sigma_{\text{inc}}$ is fixed to the value reported in Ref. [54]. The 5 GeV results are used for all nuclei except for ${}^4\text{He}$.

Target	$\omega \simeq 3 \text{ GeV}$			$\omega = 5 \text{ GeV}$		
	a [$\mu\text{b}/\text{GeV}^2$]	σ_{inc} [$\mu\text{b}/\text{GeV}^2$]	B [GeV^{-2}]	a [$\mu\text{b}/\text{GeV}^2$]	σ_{inc} [$\mu\text{b}/\text{GeV}^2$]	B [GeV^{-2}]
${}^4\text{He}$	13.1 ± 2.5	0.0	10.0 ± 3.6	—	—	—
${}^{12}\text{C}$	111.9	0.0	7.2 ± 2.5	89.7 ∓ 0.8	2.9 ± 0.8	10.0 ± 2.1
${}^{27}\text{Al}$	523.0	0.0	12.1 ± 2.1	402.8 ∓ 1.1	2.2 ± 1.1	8.1 ± 1.9
${}^{49}\text{Ti}$	—	—	—	1210.9 ∓ 1.5	9.1 ± 1.5	18.6 ± 2.1
${}^{64}\text{Cu}$	2664.0	0.0	16.5 ± 13.8	2022.4 ∓ 1.9	9.6 ± 1.9	14.6 ± 2.3
${}^{109}\text{Ag}$	8406.0	0.0	26.4 ± 3.5	6096.1 ∓ 2.8	24.9 ± 2.8	26.0 ± 2.7
${}^{197}\text{Au}$	—	—	—	20589.2 ∓ 17.4	40.8 ± 17.4	56.7 ± 8.2

precise values from the $\omega = 5 \text{ GeV}$ fit for all nuclei except for ${}^4\text{He}$ where only data at $\omega = 3.3 \text{ GeV}$ are available.

We finally reconstruct the t -dependence of the imaginary part of the Compton amplitude using Eqs. (32, 33),

$$\text{Im}\mathcal{F}_3(\omega, t) = \text{Im}\mathcal{F}_3(\omega, 0) e^{-\frac{B|t|}{2}} F_{\text{ch}}(t) \sqrt{\frac{1 + R^2(\omega, 0)}{1 + R^2(\omega, t)}}, \quad (34)$$

and estimate the ratio $R(\omega, t)$ in a Regge model. For the latter, we use a recent Regge fit [57] of the total photoabsorption cross section measured for several nuclei [58–60]. The total cross section was fitted by a sum of a Pomeron and a Reggeon exchange,

$$\sigma_{\gamma A}^{\text{tot}}(\omega) = c_P^A(\omega/\omega_0)^{\alpha_P(0)-1} + c_R^A(\omega/\omega_0)^{\alpha_R(0)-1}, \quad (35)$$

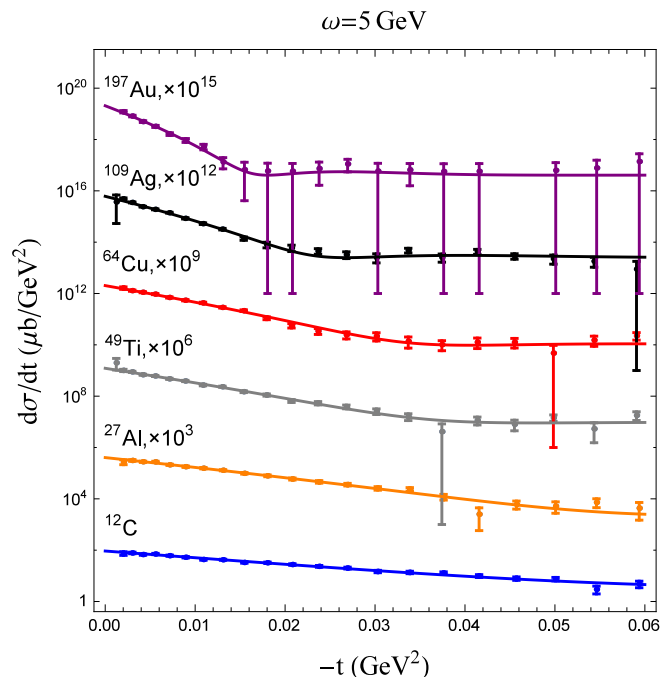


FIG. 2. Compton scattering cross section data [54] used to determine the Compton slope B compared with our fit.

with $\omega_0 = 1 \text{ GeV}$ and linear Regge trajectories $\alpha_i(t) = \alpha_{0i} + \alpha'_i t$. The intercepts are $\alpha_{0P} = 1.097$, $\alpha_{0R} = 0.5$ and the slopes $\alpha'_P = 0.25 \text{ GeV}^{-2}$, $\alpha'_R = 0.9 \text{ GeV}^{-2}$ [57]. The values of $c_{P,R}^A$ for carbon, aluminum, copper and lead are listed in Table I of Ref. [57]. From the optical theorem, $\sigma_{\gamma A}^{\text{tot}}(\omega) \propto \text{Im}\mathcal{F}_3^{\gamma A \rightarrow \gamma A}$. For a given Regge exchange contribution to an amplitude, its real and imaginary parts follow from the known phase of the Regge propagator,

$$P_R \sim e^{i\pi\alpha_R(t)} + \xi, \quad \xi = \pm 1. \quad (36)$$

For Compton scattering only the exchange with natural parity, $\xi = +1$, contributes to the spin-independent channel, and $R_i^2(t) = \cot^2[\pi\alpha_i(t)/2]$ with $i = P, R$. We found that removing the effect of the real part of the amplitude from the differential cross section to obtain the t -dependence of the imaginary part, Eq. (34), is equivalent to a change in the slope parameter B of $\approx 2.2 \text{ GeV}^{-2}$. We include this effect as an uncertainty of B , in addition to those of the fit listed in Table I, and use a simple exponential times charge form factor ansatz for the t -dependence of the amplitude $\text{Im}\mathcal{F}_3$.

Finally, our ansatz for the t -dependence of the coefficients $\mathcal{A}_1^{(0)}(t)$ and $\mathcal{A}_1^{(1)}(t)$ in front of the large logarithms at small momentum transfer t reads

$$\mathcal{A}_1^{(0,1)}(t) = \mathcal{A}_1^{(0,1)}(0) e^{-\frac{B|t|}{2}} F_{\text{ch}}(t). \quad (37)$$

While the ansatz for $\mathcal{A}_1^{(1)}(t)$ is motivated by the continuity of the function $\mathcal{A}(t, Q_1^2, Q_2^2, W^2, s)$ in t , Q^2 near the forward limit and near the real photon point, the quality of this approximation is hard to estimate. We therefore assign a 100% uncertainty to the $\mathcal{A}_1^{(1)}$ contribution.

C. Absorptive potential

The results of Eqs. (24, 30, 31), and (37) can be used to compute the absorptive potential given by Eq. (16). Using the hierarchy introduced in Eq. (24), we split the absorptive potential into two parts, $V_{\text{abs}}(r, E_b) =$

$V_{\text{abs}}^{(0)}(r, E_b) + V_{\text{abs}}^{(1)}(r, E_b)$, and find the leading and sub-leading contributions to be given by

$$\begin{aligned}
 V_{\text{abs}}^{(0)} &= c_0 \int_{\omega_\pi}^{E_b} d\omega \omega \sigma_T^0(\omega) \int_0^\infty dq j_0(qr) F_{\text{ch}}(q^2) e^{-\frac{B}{2} q^2} I_0, \\
 V_{\text{abs}}^{(1)} &= \frac{c_0}{2} \int_0^\infty dq q^2 j_0(qr) F_{\text{ch}}(q^2) e^{-\frac{B}{2} q^2} \int_{\omega_\pi}^{E_b} d\omega I_1 \\
 &\times \left\{ \left[\frac{3}{2E_b} - \frac{2}{\omega} - \frac{\omega(E_b + M)}{2ME_b^2} \right] \sigma_T^0 + \frac{\omega(E_b - \omega)}{E_b} \sigma_T' \right\}, \tag{38}
 \end{aligned}$$

with $c_0 = -\alpha m / (2\pi^3 E_b)$, $q \equiv |\vec{q}|$, $j_0(qr)$ the Bessel function of order zero, and $\omega_\pi = m_\pi + m_\pi^2 / (2M)$ the laboratory frame photon energy at the pion photoproduction threshold. The expressions for I_0 and I_1 are provided in the Appendix A.

We note that the ω -weighting $\sim \omega \sigma_T^0(\omega)$ in $V_{\text{abs}}^{(0)}$, together with the overall $1/E$ -weighting in c_0 , puts the emphasis on the photoabsorption in the hadronic energy range. Nuclear photoabsorption occurs at much lower energies and its contribution to the leading term is suppressed.

In this article, we focus on the evaluation of contributions to the absorptive potential coming from photoabsorption in the hadronic region. In the nucleon resonance region and slightly above, the total nuclear photoabsorption cross section is assumed to approximately scale with the atomic weight A as $\sigma_T(\omega) \approx A \sigma_{T,\gamma p}(\omega)$, where $\sigma_{T,\gamma p}(\omega)$ is the real photoabsorption cross section of the proton. For the evaluation of $\sigma_{T,\gamma p}^0$ and $\sigma_{T,\gamma p}'$, we use the parametrization of Ref. [61]. We point out that $\sigma_{L,\gamma p}'(\omega)$ is zero in this parametrization, hence this contribution was omitted in Eq. (38).

The naive linear A -scaling disregards the shadowing at higher energies and anti-shadowing in the resonance region (cf. Fig. 10 of Ref. [60]). Nevertheless, since Eq. (38) operates with the integrated cross section rather than the cross section itself, the two effects should largely cancel out justifying our approximation. A comprehensive study of specifically nuclear effects in photoabsorption, from the giant resonance to shadowing and anti-shadowing at hadronic energies, is postponed to a future work.

In Fig. 3, we display the result of a numerical evaluation of the two-fold integrals in Eq. (38) which determine the leading (black dashed curve) and subleading (orange dashed curve) contributions to the absorptive potential for ^{208}Pb at $E_b = 1.063$ GeV. We compare the result with the Coulomb potential (blue solid curve) of the lead nuclear charge distribution of Ref. [46] and with the Coulomb potential for a point-like charge (red dotted curve). The potentials for the point-like and the empirical charge distributions approach each other just outside the r.m.s. radius, which is ~ 5.5 fm for lead. We observe that the absorptive potential is rather small (note

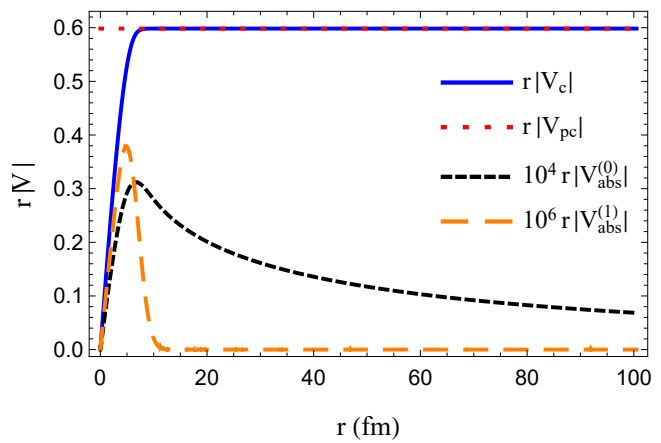


FIG. 3. The r -dependence of weighted potentials $r|V(r)|$ for ^{208}Pb as a function of r in units of Fermi. The point-charge Coulomb potential is shown by a red dotted horizontal line at $r|V_{\text{pc}}(r)| = Z\alpha$. The Coulomb potential of the empirical charge distribution corresponds to the blue solid curve. The black and orange dashed curves show the leading and subleading contributions to the absorptive potential, correspondingly, for $E_b = 1.063$ GeV.

the scale factor 10^4 in front of the leading contribution to V_{abs}) and has a finite range ($rV_{\text{abs}}(r \rightarrow \infty) \rightarrow 0$). However, it extends far outside the nuclear charge distribution as it is sensitive to scales up to the electron's Compton wave length $\sim 1/m \sim 400$ fm. This property results in a large matching distance needed for a precise evaluation of B_n . The matching distance r_m is the distance at which the total interaction potential $V(r) = V_{\text{ch}}(r) \pm iV_{\text{abs}}(r)$ has reached (within a given precision) its asymptotic value $V(r_m) = V_{\text{pc}}(r_m)$, beyond which V_{abs} can be set equal to zero. The determination of the matching distance is of crucial importance for our calculation since r_m is the distance where the numerical solution of the Dirac equation is matched to the known analytical solution with $V(r) = V_{\text{pc}}(r)$. We observe that the CPU time for the numerical calculation grows approximately linearly with r_m , and a proper balance between precision and computing time had to be found.

We studied the dependence of predictions for B_n on the matching distance for electron scattering from ^{208}Pb at $E_{\text{beam}} = 1.063$ GeV. In previous calculations for the Coulomb problem with a nuclear charge distribution of a typical radius $\lesssim 6$ fm and without including an absorptive potential, a matching distance of $r_m \sim 15$ fm had been used [21]. However, we found that the relative uncertainty of our calculation for B_n at $\theta = 5^\circ$ can not be expected to be better than 10^{-3} if r_m is chosen smaller than 120 fm. In addition, the precision of the calculation becomes worse as the scattering angle increases. The results of our calculation for B_n , which are presented in Sec. IV, are obtained with $r_m = 606$ fm. Such a matching distance represents a compromise between achieving the necessary numerical precision and keeping the calculation time under control. With $r_m = 606$ fm, the relative

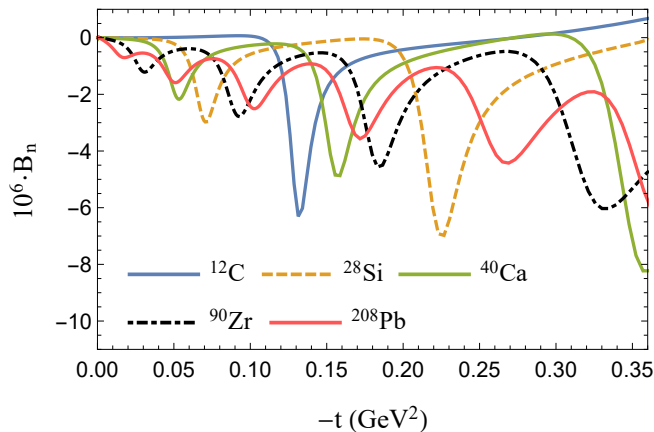


FIG. 4. BNSSA for elastic electron scattering from ^{12}C (solid blue curve), ^{28}Si (dashed orange curve), ^{40}Ca (solid green curve), ^{90}Zr (dashed-dotted black curve), and ^{208}Pb (solid red curve) versus momentum transfer squared $|t|$ at $E_b = 953$ MeV for the case when only elastic intermediate-state contributions are taken into account. For the distribution of the nuclear charge, $\rho_{\text{ch}}(r)$, we use an experimental fit of the world data on elastic electron-nucleus scattering parametrized in the form of a sum of Gaussians (^{12}C , ^{28}Si , ^{40}Ca , ^{208}Pb) or Fourier-Bessel (^{90}Zr) as reported in Ref. [46].

intrinsic numerical uncertainty of our prediction for B_n is well below $\sim 1\%$ in the range of momentum transfers considered in this paper, independently of the target and beam energy.

IV. RESULTS

In this section, we present results for B_n for electron scattering at energies ranging from 570 MeV to 3 GeV from a variety of nuclear targets. We note here that while our formalism was developed for spin-0 nuclei, for elastic scattering on an unpolarized nuclear target non-zero nuclear spin will only induce corrections of the order of the nuclear recoil, $\sim t/M^2$, which can be safely neglected.

The results of the calculation including Coulomb distortion (distorted-wave calculation, for short) of the beam-normal SSA for the case when only elastic intermediate-state contributions in the scattering process are taken into account ($V_{\text{abs}} = 0$) are displayed in Fig. 4. This figure illustrates the dependence of the asymmetry on details of the nuclear charge distribution at a fixed energy of the incoming beam, $E_b = 953$ MeV. Because the nuclear charge density is roughly represented by a nearly homogeneous sphere with a relatively sharp edge, the prediction for the beam-normal SSA features a typical diffractive pattern. The location of the first diffraction minimum gives an idea of the characteristic size of the target nucleus. One can see that for light nuclei the diffraction minima are prominent and deep, with the absolute value of the asymmetry changing by an order of magnitude in the vicinity of the minimum. For heavy

nuclei, Coulomb distortions are stronger, and the asymmetry experiences a less drastic change around the minimum. The predictions for B_n presented in Fig. 4 are in good agreement with those reported in Ref. [21].

Next we discuss results of the distorted-wave calculation of the beam-normal SSA for the case when inelastic intermediate-state contributions in the scattering process are taken into account by including the absorptive potential into the Coulomb problem. We calculate a theoretical uncertainty in several steps. First, we evaluate a relative uncertainty ϵ_1 of the asymmetry due to the uncertainty of B . The uncertainty of B receives itself two contributions: (i) the first component is the uncertainty from the fit to the Compton data and is provided in Table I; (ii) the second component is associated with neglecting the effect of the real part of the amplitude \mathcal{F}_3 in the fit of the Compton data and was estimated to be 2.2 GeV^{-2} , as discussed in Sec. III B. These two parts are combined in quadrature. Second, we evaluate a contribution ϵ_2 to the relative uncertainty of the asymmetry due to the specific choice of an ansatz for the t -dependence of the coefficient $\mathcal{A}_1^{(1)}(t)$. ϵ_2 is obtained as the relative difference between predictions for B_n computed with and without the contribution from $\mathcal{A}_1^{(1)}(t)$ to V_{abs} , while the parameter B is kept fixed at its central value. This prescription is equivalent to assigning a 100% uncertainty to the contribution from $\mathcal{A}_1^{(1)}$. Finally, the two components are added in quadrature, i.e. $\epsilon = \sqrt{\epsilon_1^2 + \epsilon_2^2}$ is used to calculate uncertainty bands shown in the following figures.

In Figs. 5 and 6, we display results for the BNSSA in the distorted-wave calculation including inelastic intermediate-states. Each curve in these figures belongs to a specific energy of the incoming beam as specified in the figure captions and a specific target nucleus as indicated on the plots. The central dashed lines correspond to the absorptive potential given by Eq. (38) and the parameter B fixed at its central value as provided in Table I (5 GeV data). The solid bands around the central lines indicate the estimated theoretical uncertainty as described in the previous paragraph. By comparing the results presented in Fig. 4 with those displayed on the left panel of Fig. 6 (both figures correspond to $E_b = 953$ MeV), we conclude that the inelastic excitations of the intermediate state provide the dominant contribution to B_n at GeV beam energies. This is consistent with the results of Ref. [24], in which only the leading-order inelastic intermediate-state excitations were considered.

In Fig. 5, we compare our prediction for B_n with the measurements by the PREX-I and HAPPEX collaborations at JLab [34] (left plot) and a series of experiments performed at MAMI [37, 38] (right plot). We note that our framework has been designed for high-energy electron scattering; apart from lacking contributions from the nuclear range, it operates with a phenomenological t -dependence motivated by the high-energy Compton scattering data. While the high-energy measurement

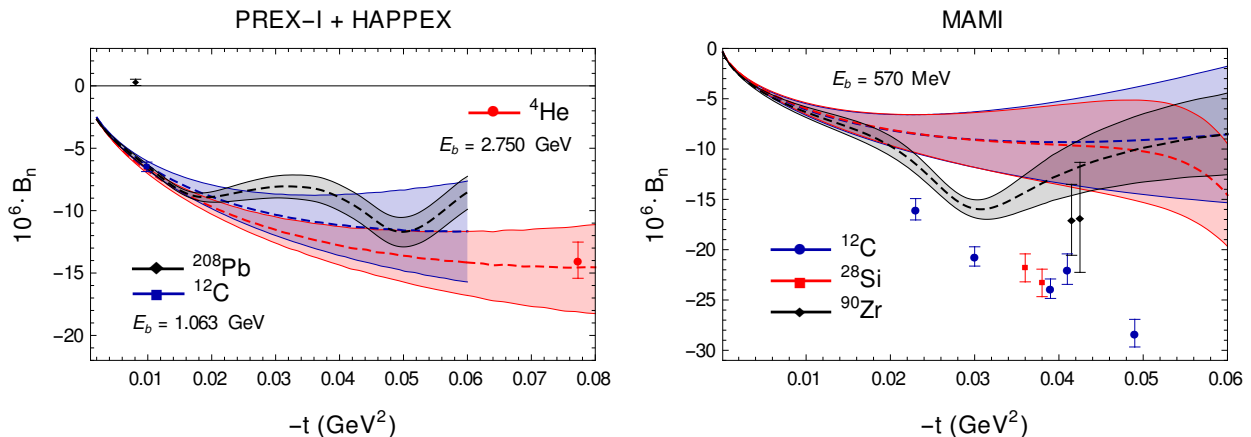


FIG. 5. BNSSA versus momentum transfer squared $|t|$ in the kinematical range where measurements are available. Left panel: Predictions for ${}^4\text{He}$ obtained with $E_b = 2.750$ GeV and for ${}^{12}\text{C}$ and ${}^{208}\text{Pb}$ with $E_b = 1.063$ GeV. Experimental data points are from the PREX-I and HAPPEX experiments [34]. Right panel: Predictions for ${}^{12}\text{C}$, ${}^{28}\text{Si}$, and ${}^{90}\text{Zr}$ obtained with $E_b = 570$ MeV. Experimental data points are from the experiments of Refs. [37, 38] at MAMI.

on ${}^4\text{He}$ by the HAPPEX collaboration at 2.75 GeV is well described, and so is a somewhat lower one on ${}^{12}\text{C}$ at 1.063 GeV, the agreement at lower MAMI energies is worse even for light and intermediate nuclei. This fact indicates that the t -dependence of the Compton cross section in the resonance region is likely not to follow the exponential fall-off as deduced from high-energy data.

The data point by the PREX-I collaboration on the ${}^{208}\text{Pb}$ target clearly stands out: the measured value of $B_n \approx +0.5$ p.p.m. does not follow the pattern of either the theoretical predictions, nor measurements on lighter nuclei, with large negative asymmetries, hence the name “the PREX puzzle”. Although the distorted-wave calculation of B_n reported here and obtained with the updated value of the slope parameter B reduces the disagreement between theory and experiment for ${}^{208}\text{Pb}$ somewhat, it is still unable to explain the origin of the sign difference between measurement and prediction.

We note that the predictions displayed in Fig. 5 are obtained using different values of the parameter B (see Table I for details) for different nuclei. These values were deduced from the Compton scattering data on 8 nuclei [53, 54]. In contrast, theoretical predictions presented in Refs. [34, 37, 38] were based on the calculation of Ref. [24] which assumed a universal parameter $B = 8 \pm 1$ GeV^{-2} , independent of the target nucleus. This value stems from the high-energy Compton data on the proton. In Ref. [24] this value was found consistent with that for ${}^4\text{He}$, thereby conjecturing that it remains constant across the nuclear chart. The present, more careful study addressed the validity of this assumption explicitly, see Table I, and found it to hold for light nuclei, from ${}^4\text{He}$ to ${}^{27}\text{Al}$. For heavier nuclei it gradually breaks down and for the heaviest nucleus, ${}^{197}\text{Au}$ the actual value of the slope is 7 times larger.

In Refs. [37, 38], light and intermediate nuclei had been studied at lower energies. In those references, the

slope B was taken universal and constant [24], but the uncertainty was assumed to be 10% (20%) of the full slope of the Compton cross section, i.e. of $B + R_{\text{Ch}}^2/3$, with the nuclear charge radius R_{Ch} . For carbon, one has $R_{\text{Ch}} \approx 2.5$ fm which leads to $B = 8 \pm 6$ (± 12) GeV^{-2} for 10% (20%) uncertainty, respectively. This is a conservative estimate in view of experimental data that allow us to reduce the uncertainty of B considerably, as shown in Table I.

Another difference between the approach of Refs. [37, 38] and the one used in the present work concerns the treatment of corrections to the leading-order behavior of the potential V_{abs} and related uncertainties. In those references, the approximate result for I_0 shown in Eq. (23) was used to obtain the central value, while the t -independent non-logarithmic term appearing in the full result of Eqs. (A4, A5), was only used to estimate the uncertainty. Here we argue that the full expression for $V_{\text{abs}}^{(0)}$ and the subleading contribution $V_{\text{abs}}^{(1)}$ are exactly calculable and should therefore be included in the central value. The leading term is model-independent as it is the only term that carries the long-range behavior $\sim \ln(|t|/m^2)$. All other corrections, including $V_{\text{abs}}^{(1)}$, are of short-range nature. Among these, $V_{\text{abs}}^{(1)}$ is the only term enhanced by the collinear logarithm $\sim \ln(4E^2/m^2)$, and its coefficient is exactly calculable, based on the low- Q^2 expansion of the near-forward virtual Compton amplitude. This enhancement justifies using 100% of this contribution as a conservative uncertainty estimate for all neglected short-range pieces.

The numerical hierarchy of parts of V_{abs} may break down upon including effects originating from low-energy nuclear excitations and the quasielastic peak. Such contributions carry a new intermediate scale $\Lambda_{\text{Nucl}} \sim 15$ MeV with $m \ll \Lambda_{\text{Nucl}} \ll E_b \sim 1$ GeV. However, as long as the beam energy is large enough ($\gtrsim 300$ MeV)

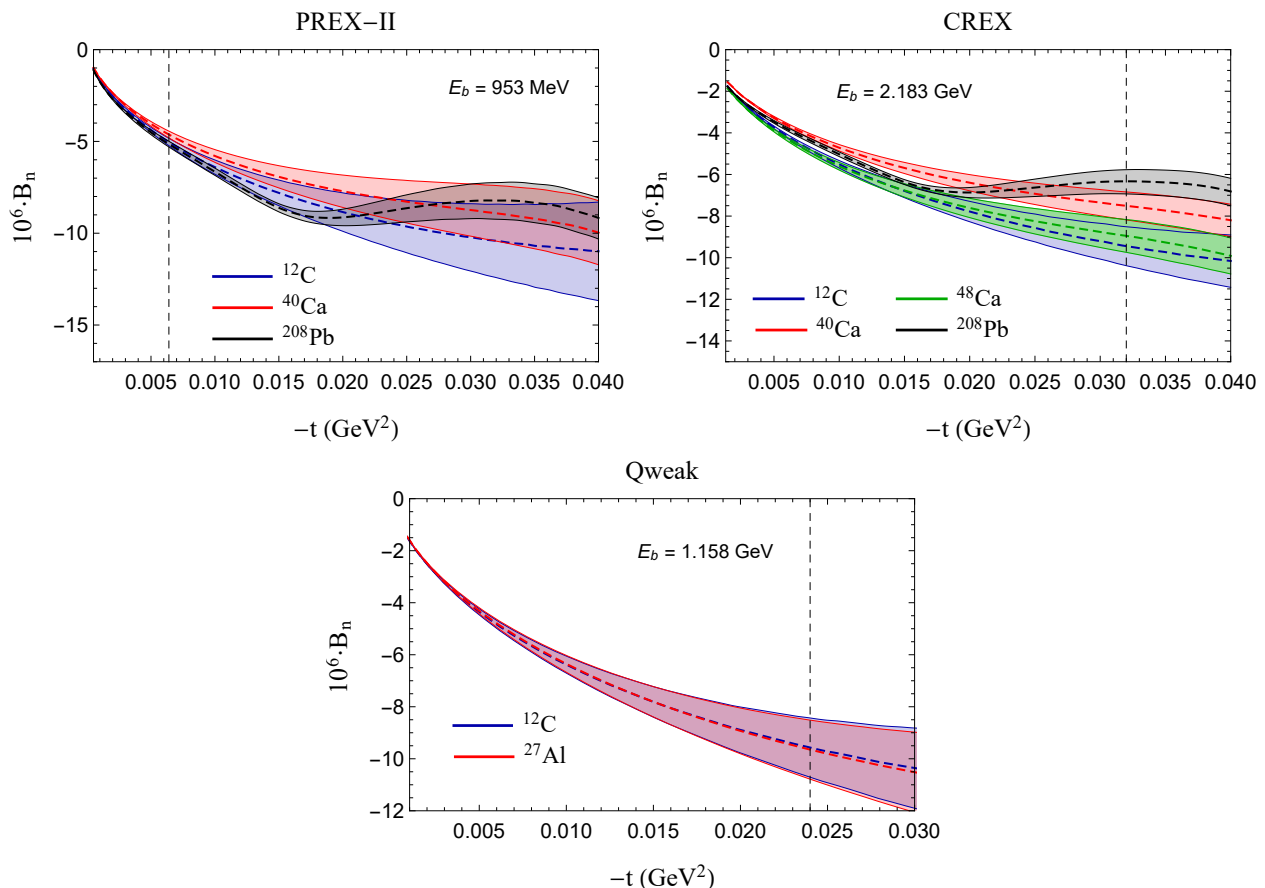


FIG. 6. BNSA versus momentum transfer squared $|t|$ for the kinematical conditions of soon-to-be published measurements. Upper left panel: Predictions for ^{12}C , ^{40}Ca , and ^{208}Pb obtained for $E_b = 953$ MeV (the PREX-II measurement [62]). Upper right panel: Predictions for ^{12}C , ^{40}Ca , ^{48}Ca , and ^{208}Pb obtained for $E_b = 2.183$ GeV (the CREX measurement [63]). Lower panel: Predictions for ^{12}C and ^{27}Al obtained for $E_b = 1.158$ GeV (the Qweak measurement). The dashed vertical lines indicate approximate values of t of the considered experiments.

the leading term $V_{\text{abs}}^{(0)}$ is exempt from a substantial modification by the contributions from such low energies. To see this we may use the approximate scaling of the integrated nuclear cross section without energy weighting, $\int \sigma_{\text{Nuc}}(\omega) d\omega = \frac{NZ}{A} \frac{\alpha}{M}$ [64], with N the number of neutrons. The expected energy-weighted result then reads, assuming $N = Z$, $\frac{1}{A} \int_0^{30 \text{ MeV}} \omega \sigma_{\text{Nuc}}(\omega) d\omega \sim \frac{\alpha \Lambda_{\text{Nuc}}}{4M} \lesssim 10^{-4}$. This is to be compared with the energy-weighted integral over the hadronic range for which we find $\int_{\omega_\pi}^{E_b} \omega \sigma_{\gamma p}(\omega) d\omega \sim 0.3$, for $E_b = 1$ GeV and using the parametrization of Ref. [61]. The effect of these nuclear contributions on the subleading term $V_{\text{abs}}^{(1)}$ remains a question which we plan to address in a future work.

In Fig. 6, we present the prediction for the kinematical conditions of soon-to-be published measurements of B_n by the PREX-II [65], CREX [66], and Qweak [67] collaborations at Jefferson Lab.

Finally, we confront the results of our distorted-wave calculation to those obtained in the plane-wave approximation as reported in Ref. [24]. Here, the BNSA is

given by

$$B_n = -\frac{2m\sqrt{|t|}}{\sqrt{(s-M^2)^2 - s|t|}} \frac{\text{Im}A_1^{2\gamma}}{A_2^{1\gamma}} \quad (39)$$

in terms of the invariant amplitudes $A_1^{2\gamma}$ (Eq. (22)) and $A_2^{1\gamma}$ (Eq. (13)). In order to perform a meaningful comparison between the two calculations, we tuned the input parameters of the plane-wave approach to be identical to the input we used for our distorted-wave calculation, i.e. instead of assuming a flat A/Z dependence of the Compton slope parameter as in Ref. [24], we used the experimental information on its $Z(A)$ dependence as summarized in Table I. In addition, instead of evaluating the asymmetry in the leading logarithm approximation, i.e. by considering only those contributions to B_n coming from approximating $\mathcal{A}_1(t)$ with $\mathcal{A}_1^{(0)}(t)$, Eq. (30), we also took into account the $\mathcal{A}_1^{(1)}(t)$ contribution to $\mathcal{A}(t)$, Eq. (31). The results of the comparison are displayed in Fig. 7. We observe that Coulomb distortion increases the absolute value of the asymmetry. While the effect

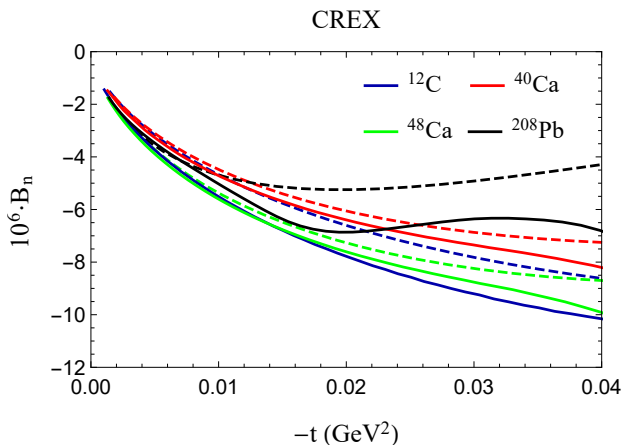


FIG. 7. BNSSA versus momentum transfer squared $|t|$ for the kinematical conditions of the CREX measurement, i.e. for $E_b = 2.183$ GeV. Dashed curves represent predictions for the asymmetry obtained in the plane-wave approximation while the solid curves correspond to the exact calculation including Coulomb distortion.

(the difference between the solid and dashed curves of the same color) may be significant, the corresponding predictions are qualitatively similar to those obtained in the plane-wave approximation.

V. CONCLUSIONS

We have computed the beam-normal single-spin asymmetry in the diffractive regime of elastic scattering of electrons from a variety of spin-0 nuclei. This asymmetry is generated by the imaginary part of the interference between the direct, $f(\theta)$, and spin-flip, $g(\theta)$, scattering amplitudes. We have evaluated these amplitudes by studying the asymptotic behavior of the solution of the relativistic Dirac equation at large distances. To realistically describe the effective interaction between the electron and target nucleus, we have employed an optical potential method. Within this approach, the electron-nucleus interaction is represented by two components of the potential: the (real) Coulomb one and (imaginary) absorptive one. The Coulomb component accounts for the contribution from elastic intermediate states in the scattering process, whereas the absorptive component describes inelastic contributions. To parametrize the absorptive component of the potential, we made use of the result for the imaginary part of the general amplitude A_1 calculated to order α^2 in the electromagnetic coupling. The corresponding perturbative calculation has been performed for the kinematics of diffractive electron scattering, where the optical theorem can be used to relate the imaginary part of the amplitude A_1 to the total photoabsorption cross section of the nucleus. To describe the t -dependence of the asymmetry near the forward scattering limit ($t=0$), we utilized information on the t -dependence

of the differential cross section of Compton scattering off nuclei at low t . Using this approach, we have obtained distorted-wave predictions for BNSSA for various spin-0 nuclei and presented the results in the kinematical range of several experiments that have been performed.

Our calculation contains several improvements with respect to earlier calculations: a) we included contributions from inelastic intermediate states into the Coulomb problem; b) we went beyond the leading logarithm approximation in evaluating B_n by considering contributions coming from $\mathcal{A}_1^{(1)}(t)$; c) we explicitly outlined the approximation scheme used for the evaluation of B_n and obtained a more realistic estimate of uncertainties. We found however that neither of these improvements seems to be enough to explain the PREX puzzle. A small and positive value of B_n obtained on a ^{208}Pb target is at variance with large negative values of B_n predicted by the theory and backed by all other measurements on light and intermediate nuclei. As a possible improvement, we plan to study contributions coming from the nuclear region of the photoabsorption cross section.

ACKNOWLEDGMENTS

The authors acknowledge useful discussions with Chuck Horowitz, Jens Erler and Stefan Wezorke. The work of M. G., O. K., and H. S. is supported by the German-Mexican research collaboration grant No. 278017 (CONACyT) and No. SP 778/4-1 (DFG). M. G. is supported by the EU Horizon 2020 research and innovation programme, project STRONG-2020, grant agreement No. 824093. X. R.-M. acknowledges funding from the EU Horizon 2020 research and innovation programme, grant agreement No. 654002.

Appendix A: Master Integrals

In this Appendix, we briefly summarize the details of the calculation of the master integrals appearing in the expression for the beam-normal SSA, Eq. (23),

$$I_0 = \frac{|t|\vec{K}^2}{2\pi} \int \frac{d\Omega_K}{Q_1^2 Q_2^2}, \quad (\text{A1})$$

$$I_1 = \frac{E|\vec{K}|}{\pi} \int \frac{d\Omega_K}{Q_1^2} = \ln \frac{4E^2 E_K^2}{m^2 E_\gamma^2}. \quad (\text{A2})$$

where $E = (s - M^2)/2\sqrt{s}$ and $E_K = (s - W^2)/2\sqrt{s}$ are the energies of the external and the intermediate electrons in the center-of-mass frame. The center-of-mass energy of the collinear quasi-real photon is $E_\gamma = E - E_K = (W^2 - M^2)/2\sqrt{s}$. The angular integration in Eq. (A1) can be performed by using the Feynman trick,

$$\int \frac{d\Omega_K}{Q_1^2 Q_2^2} = \int_0^1 dx \int \frac{d\cos\theta_x d\varphi}{[Q_1^2 + (Q_2^2 - Q_1^2)x]^2}, \quad (\text{A3})$$

and choosing the polar axis to be oriented in such a way that θ_x is the angle between \vec{K} and $\vec{K}_x = \vec{k}_1 + x(\vec{k}_2 - \vec{k}_1)$. Here \vec{k}_1 and \vec{k}_2 are the three-momenta of the initial and final electron in the center-of-mass frame. As a result, one finds [17, 18]

$$I_0 = \frac{1}{\sqrt{1 + \frac{4m^2 E_\gamma^2}{|t|\vec{K}^2}}} \ln \frac{\sqrt{1 + \frac{4m^2 E_\gamma^2}{|t|\vec{K}^2} + 1}}{\sqrt{1 + \frac{4m^2 E_\gamma^2}{|t|\vec{K}^2} - 1}}, \quad (\text{A4})$$

where we neglected terms $\sim m^2/E^2$. In the limit $m^2 \ll \vec{K}^2$, Eq. (A4) reduces to

$$I_0 = \ln \frac{|t|(E - E_\gamma)^2}{m^2 E_\gamma^2}. \quad (\text{A5})$$

-
- [1] C. E. Carlson and M. Vanderhaeghen, *Annu. Rev. Nucl. Part. Sci.* **57**, 171 (2007).
- [2] J. Arrington, P. Blunden, and W. Melnitchouk, *Prog. Part. Nucl. Phys.* **66**, 782 (2011).
- [3] M. Gorchtein, *Phys. Rev. C* **90**, 052201 (2014).
- [4] A. Afanasev, P. Blunden, D. Hasell, and B. Raue, *Prog. Part. Nucl. Phys.* **95**, 245 (2017).
- [5] O. Koshchii and A. Afanasev, *Phys. Rev. D* **96**, 016005 (2017).
- [6] P. Talukdar, V. C. Shastry, U. Raha, and F. Myhrer, *Phys. Rev. D* **101**, 013008 (2020).
- [7] H.-Y. Cao and H.-Q. Zhou, (2020), arXiv:2005.08265 [nucl-th].
- [8] I. A. Rachek *et al.*, *Phys. Rev. Lett.* **114**, 062005 (2015).
- [9] D. Rimal *et al.* (CLAS Collaboration), *Phys. Rev. C* **95**, 065201 (2017).
- [10] B. S. Henderson *et al.* (OLYMPUS Collaboration), *Phys. Rev. Lett.* **118**, 092501 (2017).
- [11] I. A. Qattan, D. Homouz, and M. K. Riahi, *Phys. Rev. C* **97**, 045201 (2018).
- [12] I. A. Qattan, S. P. Patole, and A. Alsaad, *Phys. Rev. C* **101**, 055202 (2020).
- [13] M. K. Jones *et al.* (Jefferson Lab Hall A Collaboration), *Phys. Rev. Lett.* **84**, 1398 (2000).
- [14] O. Gayou *et al.* (Jefferson Lab Hall A Collaboration), *Phys. Rev. Lett.* **88**, 092301 (2002).
- [15] J. Ahmed, P. G. Blunden, and W. Melnitchouk, *Phys. Rev. C* **102**, 045205 (2020).
- [16] A. V. Afanasev and N. P. Merenkov, *Phys. Rev. D* **70**, 073002 (2004).
- [17] A. V. Afanasev and N. Merenkov, *Phys. Lett. B* **599**, 48 (2004).
- [18] M. Gorchtein, *Phys. Rev. C* **73**, 055201 (2006).
- [19] B. Pasquini and M. Vanderhaeghen, *Phys. Rev. C* **70**, 045206 (2004).
- [20] M. Gorchtein, P. Guichon, and M. Vanderhaeghen, *Nucl. Phys. A* **741**, 234 (2004).
- [21] E. D. Cooper and C. J. Horowitz, *Phys. Rev. C* **72**, 034602 (2005).
- [22] D. Borisyuk and A. Kobushkin, *Phys. Rev. C* **73**, 045210 (2006).
- [23] M. Gorchtein, *Phys. Lett. B* **644**, 322 (2007).
- [24] M. Gorchtein and C. J. Horowitz, *Phys. Rev. C* **77**, 044606 (2008).
- [25] C. E. Carlson, B. Pasquini, V. Pauk, and M. Vanderhaeghen, *Phys. Rev. D* **96**, 113010 (2017).
- [26] O. Koshchii and A. Afanasev, *Phys. Rev. D* **98**, 056007 (2018).
- [27] O. Koshchii and A. Afanasev, *Phys. Rev. D* **100**, 096020 (2019).
- [28] A. D. Rujula, J. Kaplan, and E. de Rafael, *Nucl. Phys. B* **35**, 365 (1971).
- [29] S. P. Wells *et al.*, *Phys. Rev. C* **63**, 064001 (2001).
- [30] F. E. Maas *et al.*, *Phys. Rev. Lett.* **94**, 082001 (2005).
- [31] D. S. Armstrong *et al.* (G0 Collaboration), *Phys. Rev. Lett.* **99**, 092301 (2007).
- [32] L. Capozza, *Eur. Phys. J. A* **32**, 497 (2007).
- [33] D. Androić *et al.* (G0 Collaboration), *Phys. Rev. Lett.* **107**, 022501 (2011).
- [34] S. Abrahamyan *et al.* (HAPPEX and PREX Collaborations), *Phys. Rev. Lett.* **109**, 192501 (2012).
- [35] B. Gou *et al.*, *Phys. Rev. Lett.* **124**, 122003 (2020).
- [36] D. Androić *et al.* (QWeak), *Phys. Rev. Lett.* **125**, 112502 (2020), arXiv:2006.12435 [nucl-ex].
- [37] A. Esser *et al.*, *Phys. Rev. Lett.* **121**, 022503 (2018).
- [38] A. Esser *et al.*, *Phys. Lett. B* **808**, 135664 (2020).
- [39] D. Androić *et al.* (Qweak Collaboration), *Phys. Rev. Lett.* **111**, 141803 (2013).
- [40] D. Androić *et al.* (Qweak Collaboration), *Nature* **557**, 207 (2018), arXiv:1905.08283 [nucl-ex].
- [41] Becker, Dominik *et al.*, *Eur. Phys. J. A* **54**, 208 (2018).
- [42] C. J. Horowitz *et al.*, *Phys. Rev. C* **85**, 032501 (2012).
- [43] S. Abrahamyan *et al.* (PREX Collaboration), *Phys. Rev. Lett.* **108**, 112502 (2012).
- [44] J. Yang, J. A. Hernandez, and J. Piekarewicz, *Phys. Rev. C* **100**, 054301 (2019).
- [45] O. Koshchii, J. Erler, M. Gorchtein, C. J. Horowitz, J. Piekarewicz, X. Roca-Maza, C.-Y. Seng, and H. Spiesberger, *Phys. Rev. C* **102**, 022501 (2020).
- [46] H. D. Vries, C. D. Jager, and C. D. Vries, *Atomic Data and Nuclear Data Tables* **36**, 495 (1987).
- [47] F. Salvat, A. Jablonski, and C. J. Powell, *Comp. Phys. Comm.* **165**, 157 (2005).
- [48] F. Salvat and J. M. Fernández-Varea, *Computer Physics Communications* **240**, 165 (2019).
- [49] D. R. Yennie, D. G. Ravenhall, and R. N. Wilson, *Phys. Rev.* **95**, 500 (1954).
- [50] R. Tarrach, *Nuovo Cimento Soc. Ital. Fis.* **28**, 409 (1975).
- [51] D. Drechsel, G. Knöchlein, A. Metz, and S. Scherer, *Phys. Rev. C* **55**, 424 (1997).
- [52] V. Lensky, F. Hagelstein, V. Pascalutsa, and M. Vanderhaeghen, *Phys. Rev. D* **97**, 074012 (2018).
- [53] A. Aleksanian *et al.*, *Sov. J. Nucl. Phys.* **45**, 628 (1987).
- [54] L. Criegee, G. Franke, A. Giese, T. Khal, G. Poelz, U. Timm, H. Werner, and W. Zimmermann, *Nucl. Phys. B* **121**, 38 (1977).

- [55] X. Roca-Maza, EPL (Europhysics Letters) **120**, 33002 (2017).
- [56] C. De Jager, H. De Vries, and C. De Vries, Atomic Data and Nuclear Data Tables **14**, 479 (1974), nuclear Charge and Moment Distributions.
- [57] M. Gorchtein, T. Hobbs, J. Londergan, and A. P. Szczepaniak, Phys. Rev. C **84**, 065202 (2011), arXiv:1110.5982 [nucl-th].
- [58] D. O. Caldwell, V. Elings, W. Hesse, R. Morrison, F. V. Murphy, and D. Yount, Phys. Rev. D **7**, 1362 (1973).
- [59] D. O. Caldwell *et al.*, Phys. Rev. Lett. **42**, 553 (1979).
- [60] N. Bianchi, V. Muccifora, E. De Sanctis, A. Fantoni, P. Levi Sandri, E. Polli, A. R. Reolon, P. Rossi, M. Anghinolfi, P. Corvisiero, M. Ripani, M. Sanzone, M. Taiuti, and A. Zucchiatti, Phys. Rev. C **54**, 1688 (1996).
- [61] M. E. Christy and P. E. Bosted, Phys. Rev. C **81**, 055213 (2010).
- [62] P. Souder, R. Holmes, C.-M. Jen, L. Zana, Z. Ahmed, A. Rakhman, E. Cisbani, S. Frullani, F. Garibaldi, F. Meddi, *et al.*, Proposal for Jefferson Lab PAC **38** (2011).
- [63] J. Mammei, D. McNulty, R. Michaels, K. Paschke, S. Riordan, P. Souder, *et al.*, Proposal to Jefferson Lab PAC **39** (2013).
- [64] B. Berman and S. Fultz, Rev. Mod. Phys. **47**, 713 (1975).
- [65] D. Adhikari *et al.*, (2021), arXiv:2102.10767 [nucl-ex].
- [66] K. S. Kumar (PREX, CREX), Annals Phys. **412**, 168012 (2020).
- [67] D. Armstrong, private communication.